

# Advanced Physics Laboratory

## Alpha-Particle Spectroscopy with a Semiconductor Detector

Name: Nicolò De Masi, Manthan Chattopadhyay

Experiment Date: 11.06.2024



## Abstract

The interaction of high-energy alpha particles with air and Mylar Film is investigated using a multi-channel spectrometer. The source of alpha particles is an  $^{241}\text{Am}$  sample along with a semiconductor detector made of silicon. Upon evaluating optimal measurement conditions under vacuum, the spectrometer is calibrated according to most probable decay energies of the sample. The range of alpha particles in air is measured by varying the sample-detector distance and comparing the experimental results with theoretical values. Additionally, the energy loss of alpha particles through Mylar films of different thicknesses is measured under vacuum to calculate the stopping power, which is then compared with simulation results from SRIM.

# Contents

<b>1</b>	<b>Theoretical Background</b>	<b>4</b>
1.1	Introduction to Radioactive Decays . . . . .	4
1.1.1	Decay Law . . . . .	5
1.1.2	Decay Types . . . . .	5
1.1.3	Decay Chains . . . . .	8
1.2	Alpha Decay . . . . .	8
1.2.1	Geiger-Nuttall Law . . . . .	9
1.2.2	Quantum Tunneling of Alpha Particles . . . . .	10
1.3	Interaction of Alpha Particles with Matter . . . . .	12
1.3.1	Stopping Power . . . . .	12
1.3.2	Defining Propagation Range . . . . .	13
1.3.3	Straggling . . . . .	14
<b>2</b>	<b>Experimental Setup</b>	<b>15</b>
2.1	Surface Barrier Counter . . . . .	15
2.2	Creation of Free Charge Carriers . . . . .	16
2.3	Detector Dead Layer . . . . .	16
2.4	Energy Resolution . . . . .	17
2.5	Systematic Errors . . . . .	17
2.6	Sample Placement & Thickness . . . . .	18
<b>3</b>	<b>Results &amp; Discussion</b>	<b>20</b>
3.1	Finding Optimal Measurement Conditions . . . . .	20
3.2	Calibration of the Spectrometer . . . . .	21
3.3	Determining the Range of Alpha Particles in Air . . . . .	24
3.4	Energy Loss of Alpha Particles in Mylar Film . . . . .	26
<b>4</b>	<b>Conclusion &amp; Outlook</b>	<b>30</b>
<b>A</b>	<b>Neptunium Decay Series</b>	<b>34</b>
<b>B</b>	<b>Term Diagram of the Alpha Decay of Americium-241</b>	<b>35</b>

# 1 Theoretical Background

## 1.1 Introduction to Radioactive Decays

Radioactive decay is a stochastic process via which an unstable nucleus seeks to obtain a stable configuration. Nuclear stability is determined by the ratio of neutrons to protons. For low atomic masses, the stable ratio is approximately 1:1. At about an atomic mass of 20 this ratio increases towards 1.5:1 for the very heavy elements<sup>1</sup>. This represents a band of stability (black tiles in Figure 1), around which unstable isotopes cluster.

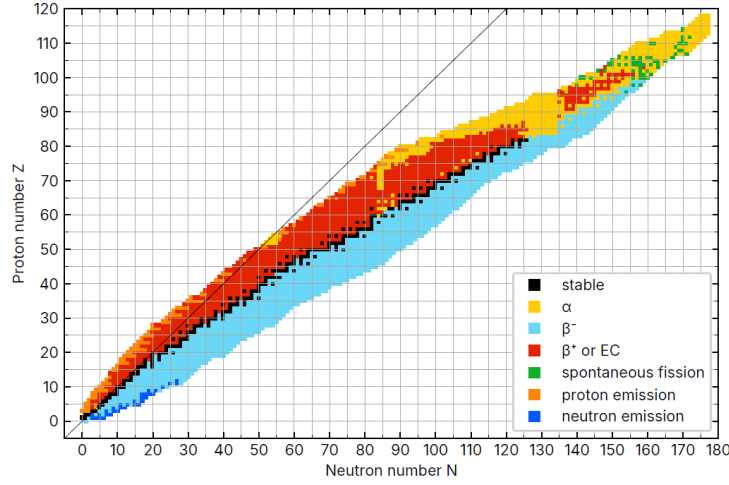
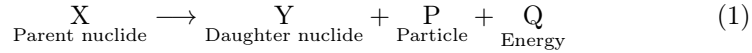


Figure 1: Nuclide chart with colour coded decays. Created from the Nubase2020 database [1]

An unstable parent nuclide X transforms into a lighter daughter nuclide Y, while emitting particle radiation P and energy Q. As a spontaneous process it is constrained to be exothermic, i.e.  $Q \geq 0$ .



This also imposes a mass constraint such that  $m_X \geq m_Y + m_P$ . The total energy released during a decay process is referred to as Q-value, resulting from the mass difference between X (in its neutral ground state) and decay products (for Y also in its neutral ground state):

$$Q = \Delta m \cdot c^2 = (m_X - m_Y - m_P) \cdot c^2 \quad (2)$$

The kinetic energies of decay products (called recoil energy in case of Y) are thus contained in the Q-value. Typically, the daughter nucleus may be in an excited state which requires emission of gamma radiation for further relaxation.

<sup>1</sup>The details of this phenomenon fall within the scope of high energy physics. However, a simplified explanation is that neutrons compensate for the high inter-proton repulsion within the nucleus.

### 1.1.1 Decay Law

Even though the disintegration of a particular parent nuclei is a stochastic process, we can predict the decay rate of an ensemble of  $N$  radioactive nuclei. If say  $x\%$  of our sample has a probability of decaying within a time interval, our measured decay will conform to this as long as our sample size is large. However, measurements will deviate from this statistical ideal as the number of radioactive nuclei drop, until eventually there will be only a single nucleus. We thus assign the decay rate  $dN/dt$  to be proportional to the number of nuclei such that

$$A = -\frac{dN}{dt} = \lambda N \quad (3)$$

where  $[A] = \text{Bq} = 1/s$  is the sample activity, and  $\lambda$  the decay constant which determines how often a decay occurs in the ensemble. Equation (3) yields,

$$N(t) = N_0 e^{-\lambda t} \quad (4)$$

where  $N_0 = N(0)$  is the initial nuclei population. Given an exponential decay, it is appropriate to define a mean life-time  $\tau$  where  $N(\tau) = N_0/e$ :

$$\tau = \frac{1}{\lambda} \quad (5)$$

We also define a half-life span  $t_{1/2}$  after which half of the nuclei will likely have decayed:

$$t_{1/2} = \frac{\ln 2}{\lambda} \quad (6)$$

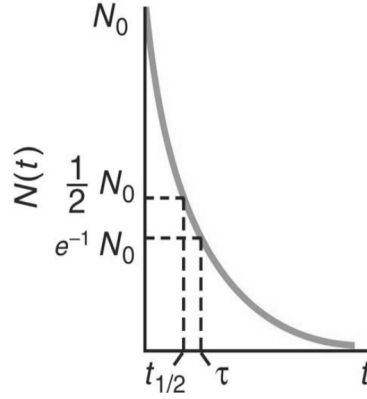


Figure 2: Exponential decay of  $N_0$  radioactive nuclei with  $\tau$  and  $t_{1/2}$  [2]

Equation (6) can be approximated as  $t_{1/2} = 0.693\tau$ . This is the fundamental basis of radiocarbon dating.

### 1.1.2 Decay Types

From Figure 1, we notice that an excess of neutrons is followed by  $\beta^-$  decay while  $\beta^+$  decay occurs for nuclei with excess protons. As we move towards heavier nuclei,  $\alpha$  decay starts to dominate. We will postpone a discussion on  $\alpha$  decay to the following section. The daughter nuclei emitted in the three main types of decay can be determined as follows:

- **$\alpha$  decay:** Emission of  ${}^4_2\text{He}$  nucleus. As both  $N$  and  $Z$  decreases by 2, the daughter nuclide is located two steps diagonally to the lower left of the nuclide chart.
- **$\beta^-$  decay:** Emission of an electron  $e^-$  and quasi-massless antineutrino with the corresponding leptonic flavor  $\bar{\nu}_e$ . A neutron of the parent nucleus is converted into a proton, thereby decreasing  $N$  by 1 and increasing  $Z$  by 1. The daughter is located one step diagonally to the upper left. The  $W$  boson facilitates this transformation by enabling the change in quark type within the nucleons.
- **$\beta^+$  decay:** Emission of a positron  $e^+$  and neutrino  $\nu_e$ . A proton of the parent nucleus is converted into a neutron, thereby increasing  $N$  by 1 and decreasing  $Z$  by 1. The daughter is located one step diagonally to the lower right.

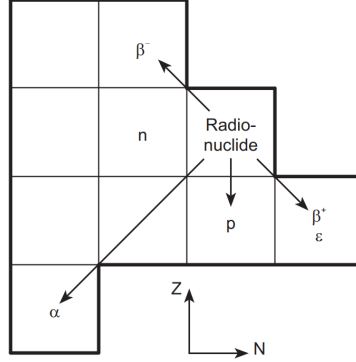


Figure 3: Radioactive decay processes on the nuclide chart. A parent with coordinates  $(Z, N)$  transforms to the daughter product through the decay process shown. [4]

In order to understand nuclear stability against  $\beta$  decay we consider the semi-empirical mass formula (SEMF) which is used to approximate nucleus mass as a function of proton and neutron number.

$$m(A, Z) = Zm_p + (A - Z)m_n - a_V A^{2/3} + \frac{a_C Z^2}{A^{1/3}} + a_A \frac{(N - Z)^2}{A} \pm \delta(A) \quad (7)$$

where  $m(A, Z)$  is mass of an atomic nucleus with  $N$  neutrons,  $Z$  protons, and therefore  $A = N + Z$  nucleons.  $m_p$  and  $m_n$  are rest masses of proton and neutron respectively, coefficient  $a_V, a_C, a_A$  are determined empirically. The sign of  $\pm\delta A$  depends on the parity of  $N$  and  $Z$  and has some power law dependence with  $A$ . For  $\beta$  decay,  $A$  remains constant but  $Z$  changes by  $\pm 1$  while  $m(A, Z)$  is quadratic in  $Z$ .

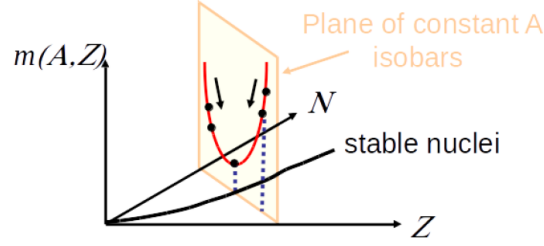


Figure 4: Determining nuclear stability against  $\beta$  decay within a plane of constant  $A$  [6]

Thus, most stable nuclide occurs when

$$\left[ \frac{\partial m(A, Z)}{\partial Z} \right]_A = 0 \quad (8)$$

Below we depict a typical situation at constant  $A$ .

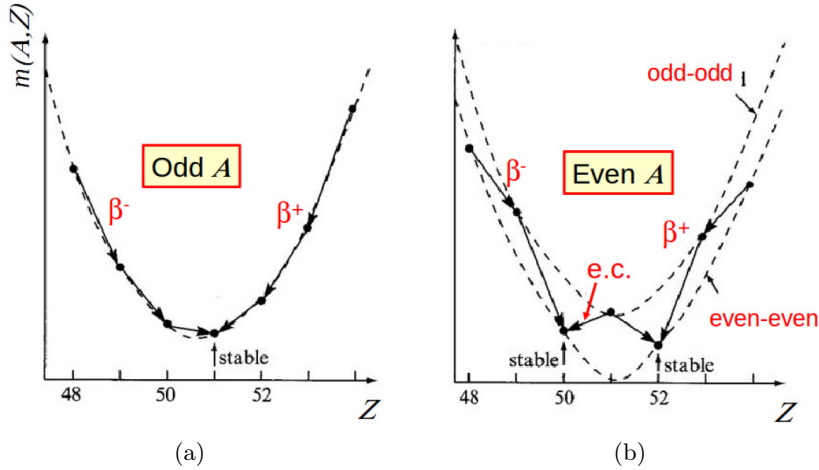


Figure 5: (a) Usually one isotope stable against  $\beta$  decay (occasionally two) and (b) Typically two even-even nuclides are stable against  $\beta$  decay (almost no odd-odd ones) [6]

Gamma decay is the third type of natural radioactive decay which involves the relaxation of a nucleus from an excited state to a lower state without changing the element.



This energy is usually carried away by emission of a photon. These photons are particularly energetic because they derive from nuclear transitions (that have much higher energies than atomic transitions involving electrons levels). The energies involved are in the order of MeV with  $\lambda$  of emitted  $\gamma$  being in  $10^{-12}$  m, thus much longer than nuclear dimensions. As gamma rays are not absorbed in air, it can be used as a spectroscopic tool for accurate energy determination,

obtaining information on the spin and parity of excited states. It is also the most important radiation used in nuclear medicine [5].

A variant of  $\gamma$  decay called internal conversion exists where an excited nucleus loses energy by emitting a virtual photon which is absorbed by an atomic  $e^-$ . This  $e^-$  is then ejected (not  $\beta$  decay as there is no change in nuclear identity).



It occurs when selection rules do not allow any multipole transition [5].

### 1.1.3 Decay Chains

Following one of the aforementioned decays, the daughter nuclei may not be in a stable state thereby undergoing a series of further decays until a stable nucleus is reached. There are mainly 2 decay methods:  $\alpha$  radiation where  $A$  reduces by 4 and  $\beta$  radiation where  $A$  remains unchanged. Thus, one obtains

$$A(n) = 4n + k \quad (11)$$

for the mass number  $A(n)$  of a nuclei in a decay chain, where  $n \in \mathbb{N}$  and  $k = 0, 1, 2, 3$  is the offset. The offset  $k$  identifies the specific natural decay chain as shown below: During the first few million years of our Solar System, these

Name of series	Thorium	Neptunium	Uranium	Actinium
Mass numbers	$4n$	$4n + 1$	$4n + 2$	$4n + 3$
Long-lived nuclide	${}^{232}\text{Th}$ ( ${}^{244}\text{Pu}$ )	${}^{209}\text{Bi}$ ( ${}^{237}\text{Np}$ )	${}^{238}\text{U}$	${}^{235}\text{U}$ ( ${}^{247}\text{Cm}$ )
Half-life (billions of years)	14 (0.08)	20 100 000 000 (0.00214)	4.5	0.7 (0.0156)
End of chain	${}^{208}\text{Pb}$	${}^{205}\text{Tl}$	${}^{206}\text{Pb}$	${}^{207}\text{Pb}$

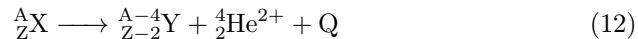
Table 1: Summary of the four decay chain pathways [7]

four chains were longer as more kinds of unstable nuclides such as  ${}^{244}\text{Pu}$ ,  ${}^{237}\text{Np}$  and  ${}^{247}\text{Cm}$  were in existence. Some of these formerly extinct isotopes are again in existence today as they have been manufactured. An important example of this is  ${}^{239}\text{Pu}$ , used in nuclear weapons, decaying to  ${}^{235}\text{U}$  via  $\alpha$  emission.

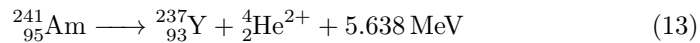
This lab uses an  ${}^{241}\text{Am}$  sample which is artificially produced in nuclear reactors, with a half life of around 432 years. It belongs to the Neptunium series with a stable nuclide of  ${}^{205}\text{Tl}$  as can be seen from Appendix A.

## 1.2 Alpha Decay

As stated in Section 1.1.2, an  $\alpha$  decay refers to emission of the sort:



For our Americium sample, the initial  $\alpha$  decay is





The total decay energy  $Q$  is distributed between the kinetic energy  $E_\alpha$  of the alpha particle and daughter nuclide  $Y$  such that:

$$Q = E_\alpha + E_Y + E_{\text{exc}} \quad (14)$$

where  $E_Y$  is the kinetic recoil energy of  $Y$ , and  $E_{\text{exc}}$  the relaxation energy of  $Y$  if it happens to be in an excited state. It is usually emitted as gamma radiation. Due to conservation of momentum:

$$m_\alpha \cdot v_\alpha = m_Y \cdot v_Y \quad (15)$$

For the alpha particle, using equation (15) yields

$$\begin{aligned} E_\alpha &= \frac{1}{2} m_\alpha v_\alpha^2 = \frac{1}{2} m_Y v_Y^2 \cdot v_\alpha \\ \implies E_\alpha &= E_Y \frac{m_Y}{m_\alpha} \end{aligned} \quad (16)$$

By applying equation (16) to equation (14) we see that the possible excitation energies  $E_{\text{exc}}$  of the daughter nuclide gauges the sharp kinetic energies of the  $\alpha$  particle. This correspondence between  $E_{\text{exc}}$  and  $E_\alpha$  can be seen from the term diagram of Americium-241 presented in Appendix B.

### 1.2.1 Geiger-Nuttall Law

A very striking feature of  $\alpha$  decay is the strong dependence of  $E_\alpha$  on radionuclide half-life (hence,  $\lambda$ ). Post Rutherford's discovery, it was documented that alpha radionuclides with shorter half-lives emitted higher-energy  $\alpha$  particles, while longer-lived nuclides emitted  $\alpha$  particles with lower energy. In 1911, Rutherford's lab assistants Hans Geiger and John Mitchell Nuttall measured the empirical relationship between decay constant  $\lambda$  and range  $R$  of  $\alpha$  particles in air [9]:

$$\log \lambda = a + b \cdot \log R \quad (17)$$

where  $a$  and  $b$  are empirical fitting parameters for a specific decay series. An illustration using data from two natural decay chains is depicted below:

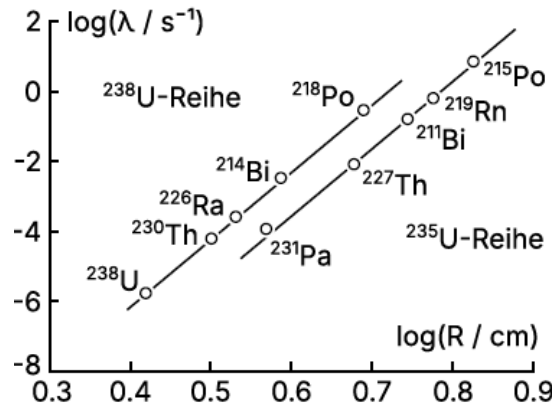


Figure 6: Geiger-Nuttall law illustrated for two natural decay chains [10]

They further found that  $R$  is proportional to cube of the particle velocity:  $R \propto v_\alpha^3$ . This yields the relation  $R \propto E_\alpha^{3/2}$  which can be substituted into equation (17) to get

$$\log t_{1/2} = \tilde{a} - \tilde{b} \log E_\alpha \quad (18)$$

where we have additionally used equation (6). This empirical law has been adjusted throughout the following decades with (Gallagher 1957) offering corrections due to hindrance-factors, and giving a relationship between  $t_{1/2}$  and decay energy  $Q$ :  $\log t_{1/2} = \tilde{\tilde{a}} + \frac{\tilde{\tilde{b}}}{\sqrt{Q}}$

### 1.2.2 Quantum Tunneling of Alpha Particles

The manifestation of quantum tunneling was first interpreted by Oscar Rice upon studying the rotationally induced dissociation of a diatomic molecule from an excited state, observed through the broadening of infrared spectral lines [11]. While being a National Research Fellow in Leipzig, Rice consulted Heisenberg, Felix Bloch, and Hendrik Kramers in order to treat the theory of this breakup and stressed the analogy with alpha decay.

The electrostatic potential between an  $\alpha$  particle and an atomic nucleus is given by

$$U(r) = \frac{2Ze^2}{4\pi\epsilon_0 r} \quad (19)$$

This relates to a potential barrier of over 9 MeV, although  $\alpha$  particles with much lower energy are observed. The potential barrier from equation (19) is depicted below:

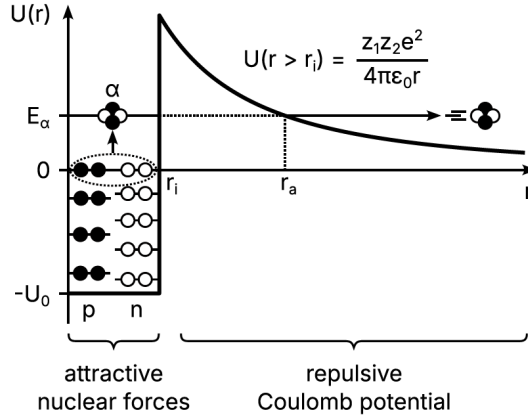


Figure 7: Potential profile at distance  $r$  from nucleus [8]

Nuclear strong force provides binding to the nucleons, however there is a finite probability that two protons and two neutrons form an  $\alpha$  particle which has much higher binding energy than the individual nucleons. Thus, the energy released from this formation excites the  $\alpha$  particle to a higher energy state  $E_\alpha$ . Classically, this energy is not sufficient to overcome the Coulomb potential barrier.

Consider an arbitrary potential  $V(x)$ :

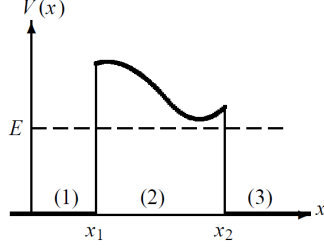


Figure 8: An arbitrary potential barrier with classically allowed zones (1) and (3) [12]

with a particle of momentum  $p_0 = \sqrt{2mE}$  incident from left. For (1) and (3),

$$\begin{aligned}\psi_1(x) &= \psi_{\text{incident}}(x) + \psi_{\text{reflected}}(x) = Ae^{ip_0x/\hbar} + Be^{-ip_0x/\hbar} \\ \psi_3(x) &= \psi_{\text{transmitted}}(x) = Ee^{ip_0x/\hbar}\end{aligned}\quad (20)$$

Since  $E < V_{\text{max}}$  in (2), we apply the WKB approximation such that

$$\psi_2(x) = \frac{C}{\sqrt{|p(x)|}} \exp\left[-\frac{1}{\hbar} \int_{x_1}^x |p(x')| dx'\right] + \frac{D}{\sqrt{|p(x)|}} \exp\left[\frac{1}{\hbar} \int_{x_1}^x |p(x')| dx'\right] \quad (21)$$

where  $p(x) = i\sqrt{2m(V(x) - E)}$ . The second term with  $D$  increases exponentially as the barrier widens is therefore unphysical. Considering a barrier wide enough that permits the approximation  $D \simeq 0$ ,  $\psi_2(x)$  becomes

$$\psi_2(x) = \frac{C}{\sqrt{|p(x)|}} \exp\left[-\frac{1}{\hbar} \int_{x_1}^x |p(x')| dx'\right] \quad (22)$$

One finds the probability corresponding to the particle's passage through the barrier via the transmission coefficient

$$T = \frac{v_{\text{trans}} |\psi_{\text{trans}}(x)|^2}{v_{\text{inc}} |\psi_{\text{inc}}(x)|^2} = \frac{|E|^2}{|A|^2} \quad (23)$$

Applying continuity of wave function and its derivative at the boundaries  $x_1$  and  $x_2$ , we eventually get an approximate value of T as

$$T \sim e^{-2\gamma}, \quad \gamma = \frac{1}{\hbar} \int_{x_1}^{x_2} \sqrt{2m(V(x) - E)} dx \quad (24)$$

When applied to our case from Figure 8,

$$T(E_\alpha) = \exp\left[-\frac{2\sqrt{2m_\alpha}}{\hbar} \int_{r_i}^{r_a} dr \sqrt{U(r) - E_\alpha}\right] \quad (25)$$

where  $m_\alpha$  is the mass of the alpha particle. Post transmission, the alpha particle will have an energy slightly below  $E_\alpha$  due to recoil of the nucleus. The term inside the exponential is called Gamow factor with an analytical solution to the integral being

$$G = \frac{2}{\hbar} \sqrt{\frac{2m_\alpha}{E_\alpha} \frac{z_1 z_2 e^2}{4\pi\epsilon_0}} \cdot \left[ \arccos\left(\sqrt{\frac{r_i}{r_a}}\right) - \sqrt{\frac{r_i}{r_a} \left(1 - \frac{r_i}{r_a}\right)} \right] \quad (26)$$

Due to the decay,  $z_1 = Z - 2$  with  $z_2 = 2$ , which enables us to represent the Gamow factor as

$$G \propto \frac{Z - 2}{\sqrt{E_\alpha}} \quad (27)$$

It follows that the mean lifetime of a particle within the potential well is  $\tau \propto 1/T \propto e^G$ . For half-life  $t_{1/2}$  a rule similar to Geiger-Nuttall law follows:

$$\ln t_{1/2} \propto G \propto \frac{1}{\sqrt{E_\alpha}} \quad (28)$$

### 1.3 Interaction of Alpha Particles with Matter

The loss of energy of an  $\alpha$  particle as it travels through a medium can mostly be attributed to two processes: (i) Coulomb interactions of the positively charged  $\alpha$  particle with the electrons of the medium (ii) Rutherford scattering of the  $\alpha$  particles with the atomic nuclei of the medium.

The Coulomb interaction is the dominant effect as alpha particles can interact with several electrons simultaneously either by exciting them to a higher energy state, or in most cases by ionizing them. These liberated electrons can have enough kinetic energy to further ionize more electrons thereby causing the so called *delta rays*. From each collision, maximum energy transfer by an alpha particle is

$$\Delta E_{\max} \approx E_{\text{kin},\alpha} \frac{4m_e}{m_\alpha} \quad (29)$$

where substituting the masses ( $m_e = 0.511 \text{ MeV}/c^2$ ,  $m_\alpha = 3727.4 \text{ MeV}/c^2$ ) result in an alpha particle transferring only 0.05% of its kinetic energy with each collision.

#### 1.3.1 Stopping Power

We define a loss of energy on a path  $x$  through a medium as the linear stopping power  $S(E)$  such that

$$S(E) = -\frac{dE}{dx} \quad (30)$$

The Bethe-Bloch formula describes the mean loss of energy per distance travelled of swift charged particles [13]. It is given as

$$-\left\langle \frac{dE}{dx} \right\rangle = \frac{4\pi z_\alpha^2 e^2}{m_e v^2} N Z \left[ \ln \left( \frac{2m_e v^2}{\langle I \rangle} \right) - \ln \left( 1 - \frac{v^2}{c^2} \right) - \frac{v^2}{c^2} \right] \quad (31)$$

where  $z_\alpha = 2$  is total charge of the alpha particle,  $Z$  the atomic number,  $N$  the number density and  $\langle I \rangle$  the mean excitation and ionizing potential of the absorbing medium. A schematic plot of stopping power shows a Bragg curve:

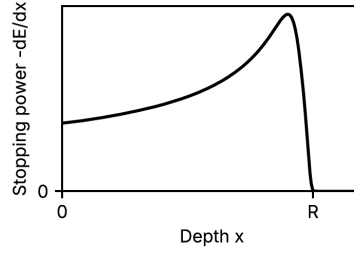


Figure 9: Stopping power as function of penetration depth within the medium. [8]

For non-relativistic speeds, the term in brackets can be considered constant which implies

$$-\frac{dE}{dx} \propto \frac{1}{v^2} \quad (32)$$

As the alpha particle propagates deeper into the medium, its speed decreases and hence an increase in stopping power as it gets more time to interact with the surrounding environment. After a certain depth, they become slow enough to absorb electrons and become neutral  ${}^2\text{He}$  atom. At this point, the stopping power drops drastically.

### 1.3.2 Defining Propagation Range

Consider the setup of a collimated alpha emitter and detector with absorption medium of thickness  $d$  placed in between. The signal at the detector produces an intensity curve as  $d$  is varied.

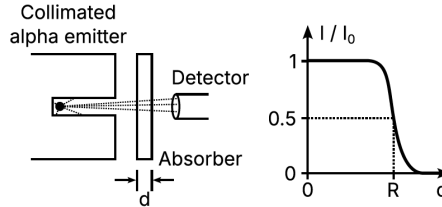


Figure 10: Schematic of setup to determine the range  $R$  [8]

Initially, complete transmission occurs for low  $d$ . After a certain thickness, the intensity at the detector decreases rapidly and creates a tail in the curve. We define the mean range  $R$  of the alpha particles in this medium as the value of  $d$  for which intensity drops to half of the initial value. An empirically determined relationship between  $R$  and  $E_\alpha$  of alpha particles is given as:

$$R(\text{cm}) = 0.318 \cdot E^{3/2} \quad (E \text{ in MeV}) \quad (33)$$

which provided minimal error in the range  $R \in [3, 7]$  cm, and applies for air temperature  $15^\circ\text{C}$  with pressure of 1010 mbar. This will provide the following curve:

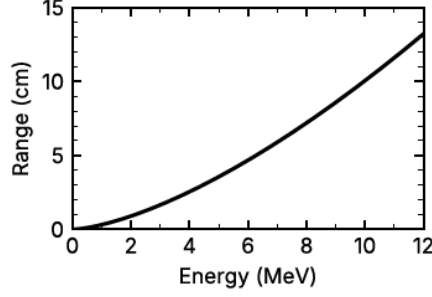


Figure 11: Range of alpha particles in air as per equation (33) [8]

### 1.3.3 Straggling

There are statistical fluctuations in the interaction and collision of alpha particles within a medium. The range  $R$  is therefore not completely predetermined but subject to a distribution that is assumed to be Gaussian:

$$P(R) = \frac{1}{\alpha\sqrt{\pi}} \exp\left\{-\frac{(R - R_0)^2}{\alpha^2}\right\} \quad (34)$$

where  $P(R)$  defines the probability distribution for the ranges surrounding a mean range  $R_0$  with  $\alpha$  defining the straggling parameter. Figure 12 shows differential and integral probability distributions for heavy particles ranges.

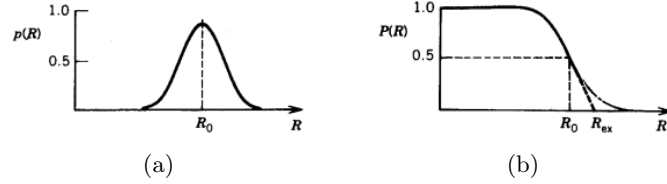


Figure 12: (a) Distribution of ranges for charged particles (b) Probability of a particle having a range larger than  $R$  [14]

The extrapolated range  $R_{ex}$  is related to straggling parameter  $\alpha$  as

$$R_{ex} - R_0 = \frac{\sqrt{\pi}}{2} \alpha \quad (35)$$

## 2 Experimental Setup

We use the Canberra Model 7401 spectrometer that includes a vacuum chamber, bias supply, preamp/amplifier, pulser, discriminator, counter, and digital display in a versatile double-width NIM [15]. As seen in Figure 13, the sample chamber contains reproducible detector-source spacing selectable from 1 to 49 mm, graduated in 4mm increments.

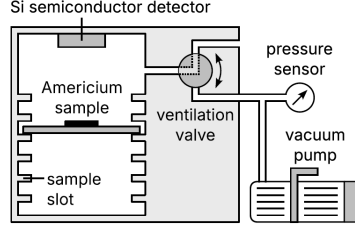


Figure 13: Schematic of the alpha particle spectrometer [8]

### 2.1 Surface Barrier Counter

The working principle of the detector can be understood by a surface barrier counter, schematic of which is presented in Figure 14.

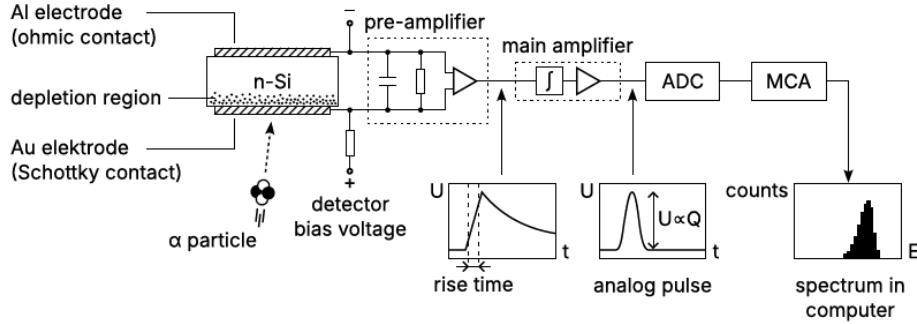


Figure 14: Schematic layout of surface barrier counter and respective electronics [8]

Our detector is made of n-doped silicon. We thus have energy levels close to the conduction band introduced due to the doping. The working principle of the detector is as follows:

- A thin layer of gold exists on the impact surface of the detector. As gold has a higher work function than silicon, free charge carriers (majority electrons due to n-doping) will naturally move from n-Si to Au. This is because electrons move from regions of higher chemical potential to regions of lower potential. This movement continues till the Fermi level of both metals equalize. The positive ionized donor atoms (remaining pentavalent atoms) are left behind near the interface. This creates an electric field that counteracts the carrier diffusion into gold. This creates a depletion region, a so-called Schottky barrier which lacks free charge carriers.

- The back side of the detector is coated with aluminium, work function of which is similar to that of n-Si. The contact is thus purely Ohmic and no depletion zone occurs. The aluminium is only used as an electrode for electrical contact. If electrons from the gold layer are removed by subjecting it to an electric potential, it is referred to as a reverse bias of the Schottky diode. This will increase the depth of the depletion layer with the Schottky barrier preventing any flow of current upon application of voltage.
- Voltage between the two electrodes builds up an electric field across the detector volume. Upon ionization via an alpha particle, an electron-hole pair is created at the depletion zone. The electron and hole get separated by this electric field and discharged into the preamplifier. This creates a steep voltage change at the capacitor of the preamplifier, which lasts until all charge carriers have been moved from detector. Shorter rise times result in faster individual pulses being resolved. It depends mostly on the detector volume and bias voltage. A much longer decay of the voltage occurs at the capacitor after this event as can be seen in Figure 14
- The preamplifier's output voltage rises and is integrated in the main amplifier, producing an analog voltage pulse whose height  $U$  is proportional to the collected charge  $Q$ . This charge  $Q$  is proportional to the alpha particle's energy. The pulse is then digitized by an analog-to-digital converter (ADC). A 12-bit ADC, for example, converts the voltage into a digital number between 0 and 4095, providing 4096 bins or channels for the energy histogram. Each alpha particle results in a digital channel number from the ADC, corresponding to the particle's energy. The Multi-Channel Analyzer (MCA) counts these events, creating and storing a histogram of the energy spectrum. To convert the spectrum's channels into energy units (keV), a calibration with a known reference energy, such as the most probable alpha decay energy of  $^{241}\text{Am}$  is performed.

## 2.2 Creation of Free Charge Carriers

For an incident alpha particle with energy  $E_\alpha$ , the number of free electrons generated  $n_e$  to a first approximation is based on the band gap  $\Delta E_g$  of the semiconductor, such that  $E_\alpha = n_e \cdot \Delta E_g$ . Thus, the energy of the alpha particle is split into a multiple of the band gap. It turns out that the band gap of Si is 1.107 eV, and it takes on average 3.62 eV to generate an electron-hole pair, thus almost a factor of 3 higher. This is due to electrons being excited to higher states in the conduction band, from which they relax by inducing phonons. This is referred to as thermalization.

## 2.3 Detector Dead Layer

The gold layer is implanted onto the detector by an ion accelerator. Thus, the gold layer can be deposited at a shallow depth below the silicon surface negating the effects of an oxide layer. However, the outer layer of the detector still experiences oxidization, along with damage during ion implantation. This disrupts the lattice structure and introduces new energy levels within the band gap that traps free charge carriers. The alpha particles will pass through this



so-called dead layer of the detector, and the carriers that get produced here can not be read out efficiently. This affects the energy resolution of the spectrometer. We will use SRIM to judge the extent to which the dead layer causes energy straggling.

## 2.4 Energy Resolution

Fluctuations due to systematic errors as discussed in the subsequent section will broaden a supposedly monochromatic energy peak. This is illustrated in Figure 15.

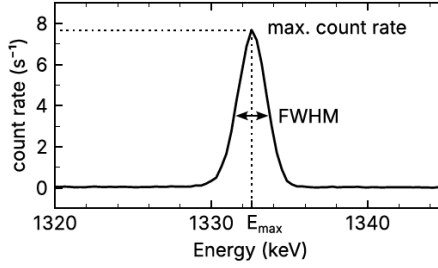


Figure 15: Broadening of a peak measured by the spectrometer [8]

We then define the energy resolution  $R$  as the resolvable line width as a proportion of the total energy  $E_{\max}$  at the peak maximum such that  $R = FWHM/E_{\max}$

## 2.5 Systematic Errors

The uncertainty in measured energy manifested as the line width has four main sources,

$$\Delta E^2 = \Delta E_i^2 + \Delta E_e^2 + \Delta E_c^2 + \Delta E_p^2 \quad (36)$$

$\Delta E_i$  is due to the intrinsic uncertainty of  $E_\alpha$  by the nucleus. This uncertainty is relatively small and can be characterized by the uncertainty principle with its canonical conjugate time such that,

$$\delta E \cdot \delta t \geq \frac{\hbar}{2\pi} \quad (37)$$

where  $\delta t$  is the lifetime of an excited state. The three remaining uncertainties are referred to as statistical uncertainties.  $\Delta E_e$  is due to the thermal noise created within the readout electronics. This can be reduced via appropriate cooling. Unsaturated chemical bonds at the interfaces and defects can capture charge carriers hindering transport. This will contribute to the charge collection uncertainty  $\Delta E_c$ . An immediate recombination event may also occur at the detector dead layer. The generation of free charge carriers itself is subject to an uncertainty  $\Delta E_p$  as alpha particles of same energy will generate different number of charge carriers due to phonon production. All error sources are Gaussian in nature except for  $\Delta E_i$  which originates from a Lorentzian distribution. For our analysis, we will perform Gaussian fits only.

## 2.6 Sample Placement & Thickness

The sample emits alpha particles uniformly in all directions, with alpha decays occurring not only on the surface but also within the sample.

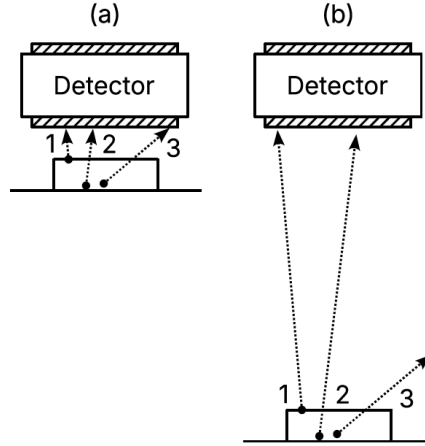


Figure 16: Effect of sample placement on detection [8]

This implies that alpha particles emitted from the sample surface (path 1 in Figure 17) can reach the detector with negligible energy loss while traveling through the vacuum chamber. In contrast, alpha particles generated inside the sample (paths 2 and 3 in Figure 17) will interact with the sample material, losing energy before exiting the sample.

This results in an asymmetric peak in the spectrum, where the low-energy left edge is significantly broadened by alpha particles that have lost energy within the sample. The high-energy right edge is less broadened and can be attributed to the systematic statistical uncertainties which we have covered in the previous section.

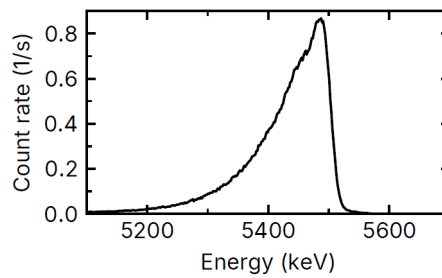


Figure 17: Expected asymmetry in the spectrum of  $^{241}\text{Am}$  [8]

The distance between the sample and the detector also impacts the spectrum quality. When the sample is positioned very close to the detector (Figure 17 (a)), almost all emitted alpha particles are detected, resulting in a high count rate. When the sample is placed farther from the detector (Figure 17 (b)), most alpha particles miss the detector, leading to a lower count rate.

Additionally, the positioning affects the peak broadening in the spectrum as well. Close to the detector, alpha particles emerging from the sample at shallower angle are counted. These particles have interacted with a substantial amount of sample material and lost corresponding energy. At greater distances, shallow-angled alpha particles miss the detector, and only those hitting the detector surface almost perpendicularly are registered. The path that these alpha particles have traversed will correspond to the vertical extent at most. With increasing distance, the spectrum peak becomes narrower as shallow-angled alpha particles are excluded. Our results in the following section will reflect these observations.

### 3 Results & Discussion

#### 3.1 Finding Optimal Measurement Conditions

We find the optimal distance between the detector and our sample for which, we have the maximum intensity while maintaining a sufficient resolution.

The characteristic spectrum of our  $^{241}\text{Am}$  sample for 7 different distances  $\in [3, 27]$  mm is measured. All measurements are performed under a vacuum and detector voltage of 80 V.

As discussed in Section 2.6, we gauge the quality of the curves by calculating FWHM. Due to the systematic errors covered in Section 2.5, we get asymmetrically broadened peaks for the lower energies. We thus perform a Gaussian fit for the right half of the curves.

$$f(x) = ae^{-\frac{1}{2}\left(\frac{x-b}{c}\right)^2} \quad (38)$$

The parameters represent:

- $a$  = height of the curve's peak
- $b$  = position of the center of the peak
- $c$  = standard deviation  $\sigma$

We thus find:

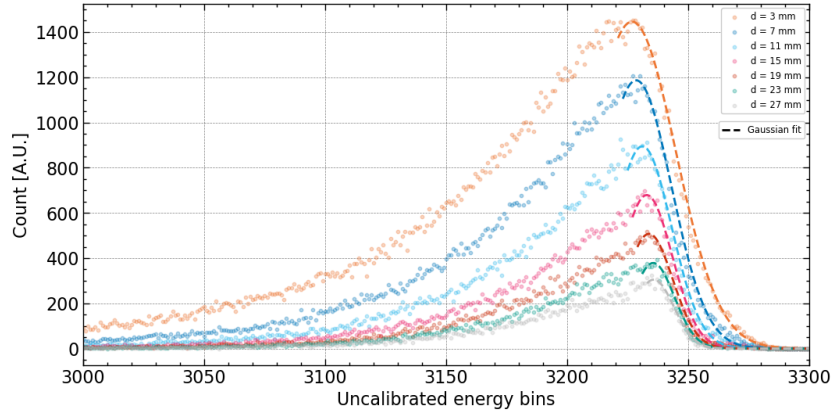


Figure 18: Spectrum of  $^{241}\text{Am}$  sample with finite thickness and asymmetrically broadened peak along with Gaussian fits for 7 distances to the detector. The energy position of the x axis has not been calibrated, as it slightly shifts for different distances, and is unnecessary for the scope of the task.

The fitting parameters give us all the information to find the optimal measurements:  $a$  gives us the maximum intensity of each curve, while  $c \equiv \sigma$  for a normal distribution is related to the FWHM by:

$$\text{FWHM} = 2\sqrt{2\ln 2}\sigma \quad (39)$$

We plot both the Intensity and FWHM with respect to the distance and perform an interpolation. At the optimal distance, we require maximum intensity

and minimal FWHM such that the resolution  $R$  as defined in Section 2.4 is maximized.

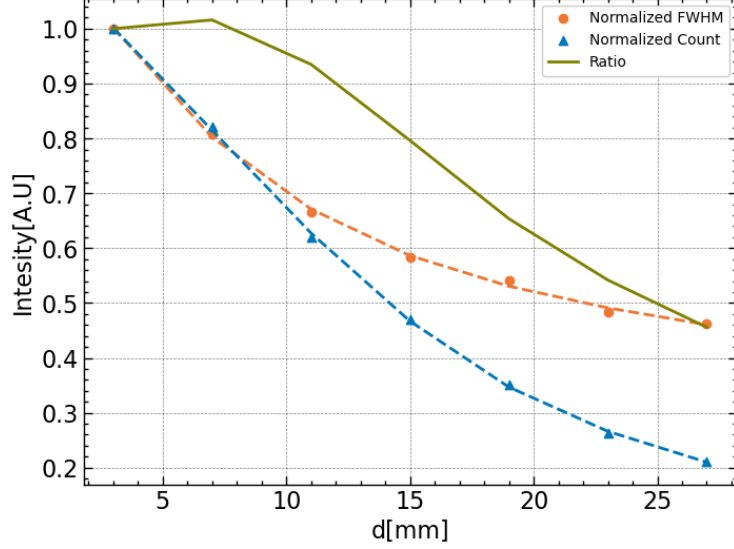


Figure 19: Behaviour of maximum intensity and FWHM of the curves from Fig. 18 with respect to  $d$ . Both curves have been normalized to  $d=3$  mm

Figure 19 shows that the optimal distance of the sample to the detector is at 7 mm. For higher distances, the sharp drop in intensity does not justify the decreased FWHM.

### 3.2 Calibration of the Spectrometer

The Analog-to-Digital Converter (ADC in Figure 14) converts the output voltage into a series of subsequent bins (channels), each corresponding to a different energy. The Multi-Channel Analyzer (MCA in Figure 14) counts every event, assigning it to the appropriate channel and returns a frequency spectrum.

The retrieved data is thus a frequency count of a specific set of unknown energy bins: we are given no information about the exact energies themselves, but only on the general reciprocal behavior. A further calibration of energy axis aided by Appendix A is required. We list the  $E_\alpha$  with highest probability:

- $E_0 = 5485.6 \text{ keV}$  (p=84.8 %)

The available bits in the ADC produces 4096 ( $2^{12}$ ) energy bins, each corresponding to a certain energy of the incoming  $\alpha$  particle, with the most intense one representing the most probable energy. For calibration, knowledge of the channel width is required, i.e. the minimum resolvable energy difference. Ideally, one would consider two or more known energy points and run a linear calibration based on channel position: of the resulting parameters, the slope will describe the exact channel width.

$$E_{\text{known}} = a * x_{\text{channel}} + b \quad (40)$$

Unfortunately, we only have one known energy data, with an associated channel number (in reference to the figure below):  $x_{E_0} = 3235$ .

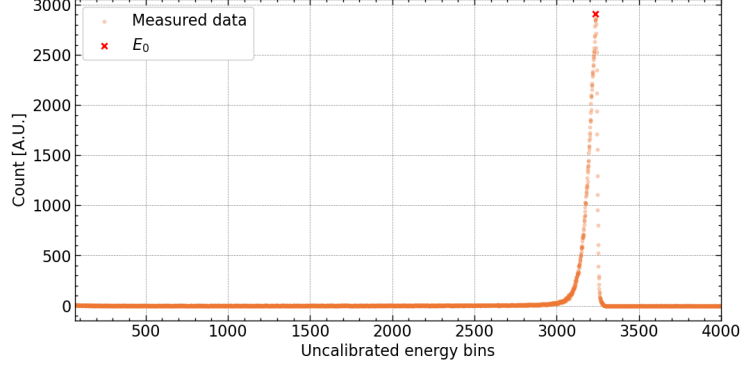


Figure 20: Uncalibrated energy spectrum

To calibrate our energies, we then (imprecisely) assume  $b=0$ . Then the channel width ( $a$ ) is easily found by:

$$C.W. \equiv a = \frac{E_0}{x_{E_0}} = \frac{5485.6 \text{ keV}}{3235} = 1.6957 \text{ keV} \quad (41)$$

The energy axis will be re-calibrated accordingly:

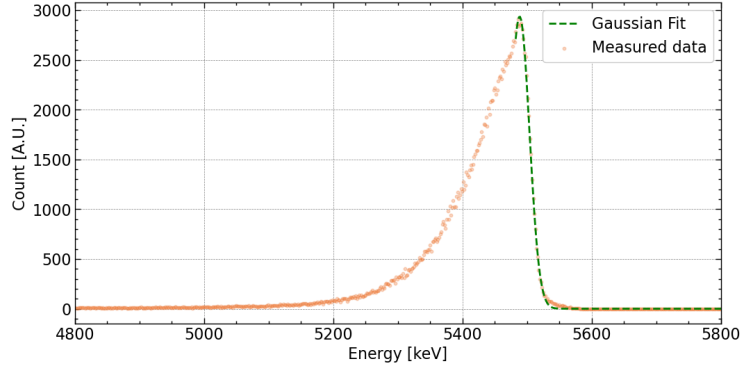


Figure 21: Calibrated energy spectrum, with Gaussian fit

The Gaussian fit from Figure 21 yields:  $\text{FWHM} = 35.84 \pm 0.16 \text{ keV}$ . According to Section 2.4, the energy resolution will be:

$$R = \frac{\text{FWHM}}{E_{\text{max}}} = \frac{35.84 \pm 0.16}{5485.6} = (6.53 \pm 0.03) \times 10^{-3} \quad (42)$$

The detector has a 50 nm thick silicon dead layer that is responsible for some energy loss. We use the SRIM to simulate energy straggling inside the 50 nm dead silicon layer:

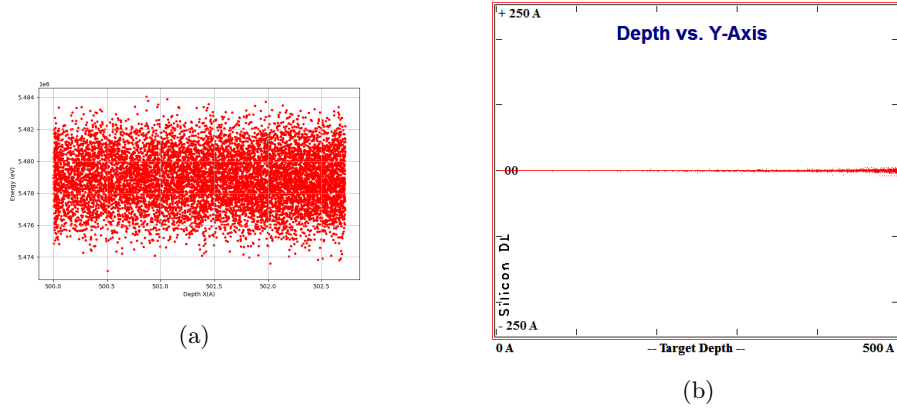


Figure 22: (a) Final spread of energy against depth after traversing through dead layer and (b) Implantation of the alpha particles within the 50 nm dead layer.

We simulate  $N = 9999$  alpha particles with initial energy of 5.48 MeV corresponding to the most probable  $E_\alpha$  of our sample. A histogram along with a Gaussian fit to analyze the spread of energy losses among our particles is presented below:

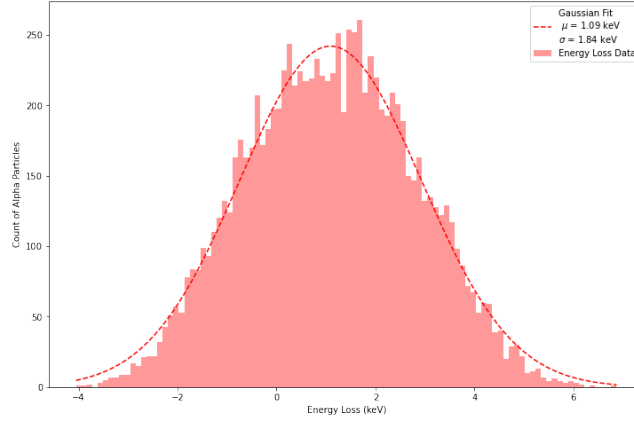


Figure 23: Alpha particle count against energy loss of alpha particles after traversing through dead layer. A bin number of 100 was chosen.

The number of bins  $k$  was set to the square-root choice [16],

$$k = \left\lceil \sqrt{N} \right\rceil = 100 \quad (43)$$

which yielded a mean energy loss of 1.09 keV and a standard deviation of 1.84 keV. Thus, the percentage of experimentally determined FWHM caused by energy straggling within the dead layer can be determined by:

$$\frac{\text{FWHM}_{\text{straggling}}}{\text{FWHM}_{\text{exp}}} = \frac{2\sqrt{2 \ln(2)} 1.84}{35.84} = 0.121 \quad (44)$$

Even though the mean loss of  $E_\alpha$  within the dead layer is around 1.09 keV which amounts to only 0.2%, the standard deviation of energy losses is almost double the value. This results in a contribution of around 12.1% to the experimentally determined FWHM.

### 3.3 Determining the Range of Alpha Particles in Air

We now find the maximum range of alpha particles in air by varying the distance between the sample and detector such that, we observe the loss in energy of the particles due to interaction with air. We will maintain calibration outcomes from previous sections. We resort to a Gaussian fit to the right half of energy spectrum for different sample distance  $d$ .

If one were to simply take the index of the most intense channel, the general behaviour of the Energy to Distance relationship would still be clear but substantially less accurate, as the stochastic aspect to the measurement would be completely ignored (and the resulting errors that come with it). By fitting the Gaussian distributions instead, the following behaviour is observed:

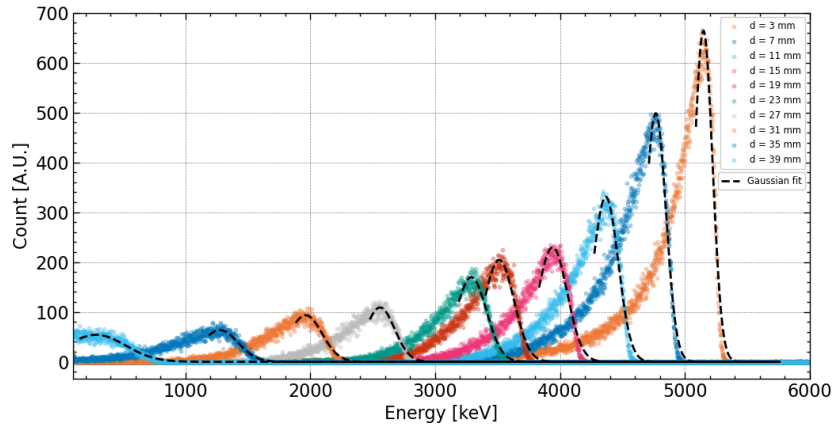


Figure 24: Energy spectrum with Gaussian fit for different distances between detector and sample  $d$

From Fig. 24 we observe that the maximum energy of the detected incoming  $\alpha$  particles decrease substantially with  $d$ . The fit yields the following values:



$d[mm]$	$E_{\max}[keV]$
3	$5148.91 \pm 0.81$
7	$4767.22 \pm 0.74$
11	$4366.69 \pm 0.76$
15	$3940.85 \pm 0.85$
19	$3513.14 \pm 0.85$
23	$3289.77 \pm 0.71$
27	$2559.33 \pm 0.83$
31	$1962.89 \pm 1.01$
35	$1276.39 \pm 1.20$
39	$285.56 \pm 2.06$

Table 2: Table of  $d$  vs.  $E_{\max}$

The errors associated with the energies are also a good indicator of the general behaviour of our data, as they get relatively bigger for bigger  $d$ , due to the increased variance of our data.

We now plot  $d$  vs.  $E_{\max}$ . The energy errors are visually omitted, as they are substantially smaller than the true values, but are employed in the calculations.

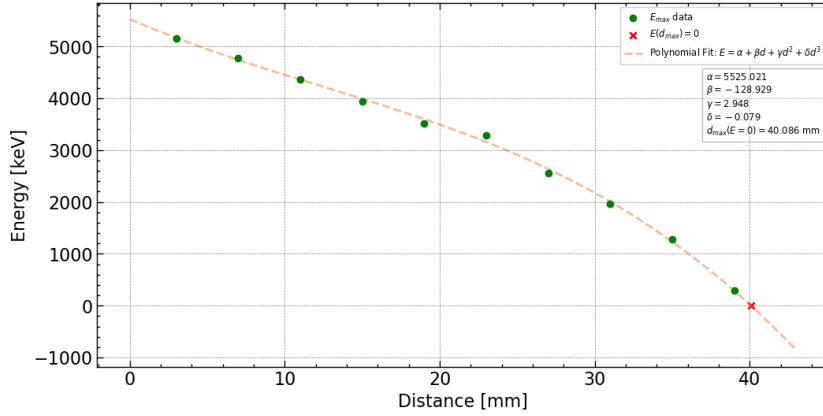


Figure 25:  $E_{\max}$  against  $d$  plot, with polynomial fit.

A polynomial fit allows us to find the general scaling law between the two and extrapolate the distance at which the particles would go completely undetected. We find that to be:

$$R_{\text{ext}} = d_{\max}(E = 0) = 40.086mm \quad (45)$$

According to equation (33), we can estimate the maximum range  $R$  of the alpha particles. We find  $R$  first in terms of the theoretical energy of the most probable transition  $E_0 = 5.486$  MeV:

$$R_{\text{th}} = 0.318E_0^{\frac{3}{2}} = 46.83mm \quad (46)$$

Alternatively, the parameter  $\alpha$  from the fit in Fig 25 represents the initial Kinetic Energy of the particles in the hypothetical circumstance that the sample was

found at at distance  $d = 0$  to the detector, i.e. with no loss of energy. This we find to be:  $\alpha = E_{0,fit} = 5525.02 \text{ keV} = 5.525 \text{ MeV}$ , from which we calculate the range to be:

$$R_{fit} = 0.318 E_{0,fit}^{\frac{3}{2}} = 41.30 \text{ mm} \quad (47)$$

Thus, both the extrapolated  $R_{ext}$  and fitting parameter  $\alpha$  underestimates  $R$  by on average 13% of the theoretical predicted value.

We can additionally simulate the behaviour of alpha particles in air with the SRIM program once again and obtain the following:

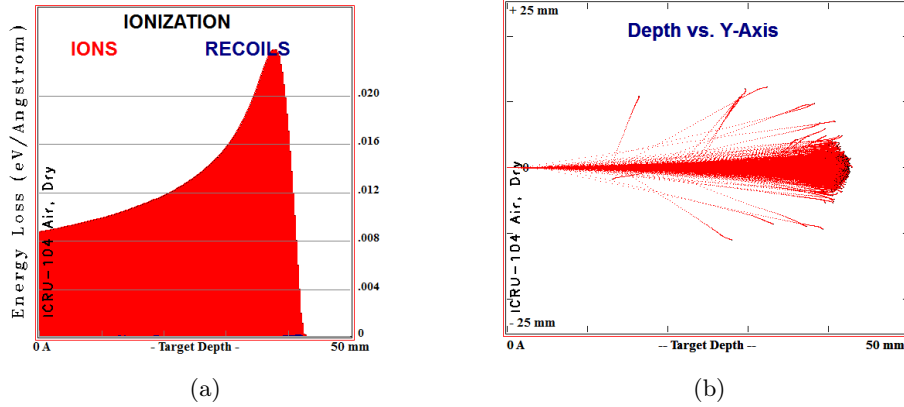


Figure 26: (a) Energy loss (stopping power) of  $\alpha$  particles in air vs distance from the sample and (b) visual representation of alpha particles scattering in air.  $N = 9999$  and  $E_{initial} = 5.48 \text{ MeV}$  with 50 mm air volume at standard conditions.

According to Fig. 26 (b), the distance at which the energy loss falls to 0, is 43.5 mm. This is in good accordance with our result with  $R_{fit}$  being the closest with an offset of only 5%.

### 3.4 Energy Loss of Alpha Particles in Mylar Film

We evaluate the energy loss of alpha particles as they pass through different materials, as it is crucial for various applications in both nuclear physics and material science. One such material of interest is Mylar, a type of thin film made from Polyethylene Terephthalate (PET), commonly used in various industrial and scientific applications due to its mechanical strength, chemical stability, and insulating properties. In its metal-coated variant with a thickness of  $12 \mu\text{m}$  it can be used for emergency blankets to ward off hypothermia.

We measure the energy loss of alpha particles as they traverse through Mylar films of varying thicknesses, and we do this while maintaining a constant sample detector distance under a vacuum, such that we have optimal conditions and minimal errors. The Mylar films available to us were combined to give 13 thicknesses ranging from 2.5 to  $26.5 \mu\text{m}$ . For each, we take a measurement of the energy spectrum (which we will calibrate accordingly similar to previous sections) and obtain the following:

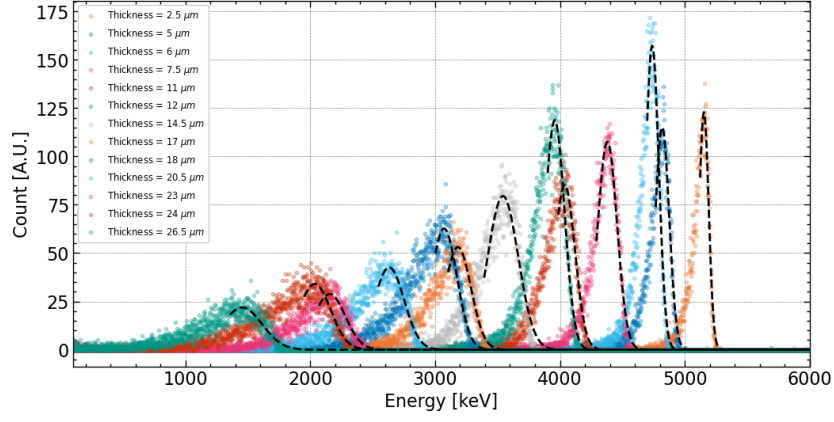


Figure 27: Energy spectrum Gaussian fit with Mylar films of varying thickness

Each Gaussian fit gives a central maximum energy:

$Thickness[\mu m]$	$E_{\max}[keV]$
2.5	$5153.13 \pm 0.30$
5	$4818.80 \pm 0.44$
6	$4738.61 \pm 0.45$
7.5	$4379.78 \pm 0.51$
11	$4038.30 \pm 1.05$
12	$3958.22 \pm 0.75$
14.5	$3543.32 \pm 1.14$
17	$3182.76 \pm 1.32$
18	$3072.24 \pm 1.25$
20.5	$2632.36 \pm 1.66$
23	$2155.75 \pm 2.25$
24	$2035.82 \pm 2.18$
26.5	$1455.04 \pm 3.55$

Table 3: Mylar film thickness vs.  $E_{\max}$

We now perform a third order polynomial fit of  $E_{\max}$  against thickness  $t$ :

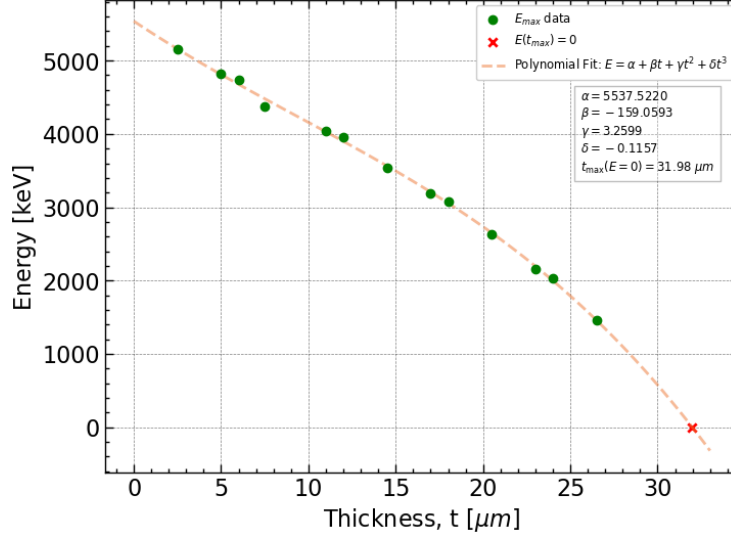


Figure 28: Mylar film thickness vs.  $E_{\max}$  with Polynomial fit.

We note minimal third order contribution with mostly a quadratic behavior. The lack of data past  $26 \mu\text{m}$  for the tail (as seen in Fig. 10) led to speculative measures of the thickness range, i.e., the projected minimum thickness of the Mylar films for which the energy drops to 0.

Regardless, the stopping power of Mylar will be subsequently calculated from the fitting equation. As defined in Section 1.3.1,  $S$  represents the rate of energy loss per unit distance traveled by the alpha particles within the film. Applying equation (30) to the parameters found in the polynomial fit, we get:

$$S(t) = -\frac{dE(t)}{dt} = -\beta - 2\gamma t - 3\delta t^2 \quad (48)$$

Plotting  $S$  against the thickness  $t$  we find:

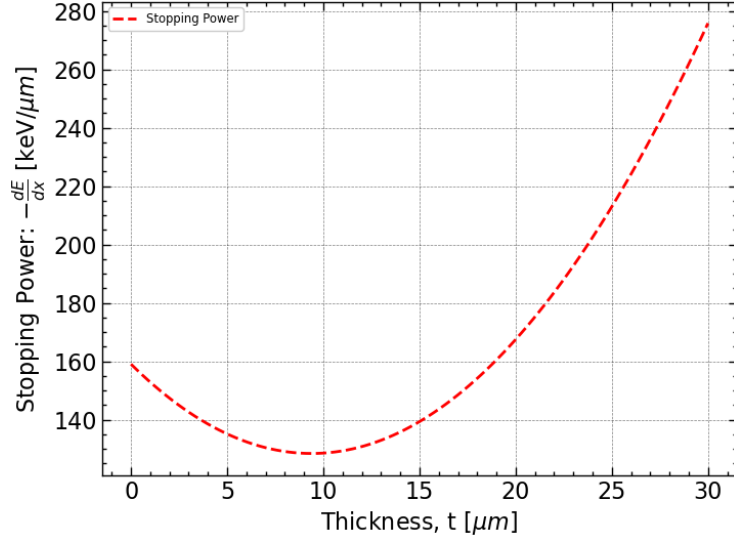


Figure 29: Mylar film stopping power vs its thickness

The region where stopping power decreases sharply (giving the so called Bragg curve), is absent due to lack of the tail in Figure 28 as discussed prior.

This is clearer when compared with SRIM data, for which the behaviour of the stopping power is the following:

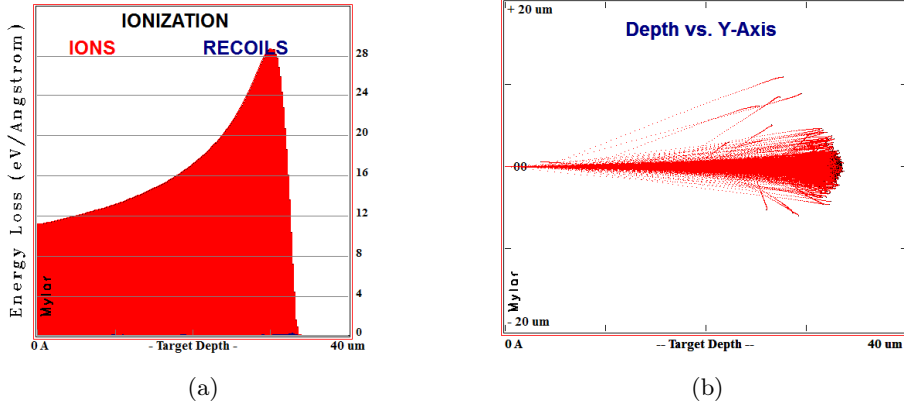


Figure 30: (a) Energy loss of  $\alpha$  particles in Mylar film vs thickness according to a SRIM simulation and (b) visual representation of  $\alpha$  particles in Mylar films.

It is often the industry standard to find stopping power  $S$  in dependence with ion energy. Given alpha particles with initial energy  $E_0$ , we calculate the remaining energy  $E(t)$  at a given thickness  $t$  by,

$$E(t) = E_0 - \int_0^t \left( \frac{dE}{dt} \right) dt \quad (49)$$

As our experimental data is not dense enough for a discretized numerical integral, we apply equation (49) to our fitting equation (48) and obtain the following

curve for  $t \in [0, 30] \mu m$ :

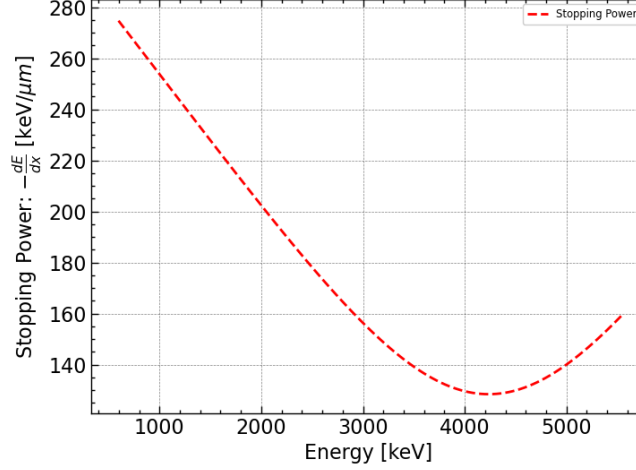


Figure 31: Stopping power for alpha particles of different energies in Mylar films

For high energies, low stopping power is expected due to lowering of interaction time as discussed in Section 1.3.1. We expect a Bragg peak prior to the 1 MeV range which occurs just before the particle comes to rest and corresponds to maximum energy transfer to the material. The dominant process near the Bragg peak is ionization with significant momentum transfer to the material's electron cloud. Further reduction in energy reduces stopping power due to the particle losing ability to ionize atoms, thereby only causing minor elastic collisions. A verification of this behavior is provided in [17].

## 4 Conclusion & Outlook

Upon exploring radioactive decays, a focus was made on alpha particles and their interaction with matter. We derived the optimal measurement conditions of our spectrometer by analyzing intensity and FWHM for different source-detector distances which offered an optimization problem for maximizing resolution. At the found optimal distance of 7 mm, we calibrated the spectrometer's energy frequency distribution, resulting in a channel width of 1.7 keV. The rest of the measurements were calibrated accordingly. A histogram analysis of SRIM data for the silicon dead layer of the detector yielded a mean energy loss of 1.09 keV with a standard deviation of 1.84 keV, contributing significantly to the FWHM by approximately 12.1%.

By opening the ventilation valve, the range of alpha particles in air were evaluated by performing Gaussian fits to the energy spectrum for different source-detector distances. A polynomial fit with mostly quadratic contribution was obtained for maximum energy vs. distance travelled in air. The maximum ranges found were the following:

- $R = 40.086$  mm: polynomial fit extrapolation
- $R_{th} = 46.83$  mm: equation (33) w.r.t. the known most probable energy

- $R_{\text{fit}} = 41.30$  mm: equation (33) w.r.t. the estimated initial energy from the fit (closest to SRIM data)
- $R_{\text{SRIM}} = 43.50$  mm: according to SRIM data

Lastly, Mylar foils of different thicknesses were placed between detector-sample path and the energy losses analyzed by extrapolating the stopping power function and comparing it to SRIM data. We observe the same increase in stopping power for thicknesses up to  $\approx 25\mu\text{m}$ , but fail to capture the tail-end behavior and intensity drop due to a lack of data closer to the critical thickness. We were unable to find accurate dependence of stopping power  $S$  with respect to the ion energy using discretized numerical integration due to the same reason. However, its general behavior was still captured.

We stress the importance of obtaining more data near the critical thickness of Mylar foils around  $30\mu\text{m}$ . Additionally, utilizing multiple known energy points for calibration can improve accuracy and reduce uncertainties associated with single-point calibration.

## References

- [1] F.G. Kondev, M. Wang, W.J. Huang, S. Naimi, and G. Audi. The NUBASE2020 evaluation of nuclear physics properties. Chinese Physics C, 45(3):030001, March 2021. doi:10.1088/1674-1137/abddae. (URL:<https://www-nds.iaea.org/amdc/>)
- [2] Braunstein G. Nuclear Physics. University of Florida. (URL:<https://physics.ucf.edu/~gabriel/Nuclear%20Physics.pdf>)
- [3] *Alpha Particle Spectroscopy*. (URL:<https://ph.qmul.ac.uk/sites/default/files/PLAB%20-%20Ex%201%20Alpha%20particle%20spectroscopy.pdf>)
- [4] Soti, Zsolt & Magill, Joseph & Dreher, Raymond. (2019). Karlsruhe Nuclide Chart – New 10th edition 2018. EPJ Nuclear Sciences & Technologies. 5. 6. 10.1051/epjn/2019004.
- [5] Prof. Cappellaro (2012). Introduction to Applied Nuclear Physics. MIT OpenCourseWare. (URL:<https://ocw.mit.edu/courses/22-02-introduction-to-applied-nuclear-physics-spring-2012/>)
- [6] Prof. Potter. Nuclear Decay. University of Cambridge. (URL:[https://www.hep.phy.cam.ac.uk/~chpotter/particleandnuclearphysics/Lecture\\_15\\_NuclearDecay.pdf](https://www.hep.phy.cam.ac.uk/~chpotter/particleandnuclearphysics/Lecture_15_NuclearDecay.pdf))
- [7] Davis, A. M. (2022). Short-lived nuclides in the early solar system: Abundances, origins, and applications. Annual Review of Nuclear and Particle Science, 72(1), 339–363.
- [8] Plotzki, D. (2024). Alpha Particle Spectrometry with a Semiconductor Detector. Advanced Physics Laboratory. Leipzig University. (URL:[https://home.uni-leipzig.de/physfp/versuche/alp\\_e.html](https://home.uni-leipzig.de/physfp/versuche/alp_e.html))
- [9] H. Geiger and J. M. Nuttall. LVII. The ranges of the  $\alpha$  particles from various radioactive substances and a relation between range and period of transformation. The London, Edinburgh, and Dublin Philosophical Magazine and Journal of Science, 22(130):613–621, October 1911. doi:10.1080/14786441008637156.
- [10] Wolfgang Demtröder. Alphazerfall. In Experimentalphysik 4: Kern-, Teilchen- und Astrophysik, chapter 3, page 45. Springer, 4th edition, 2014. ISBN 978-3-642 21475-2. doi:10.1007/978-3-642-21476-9.
- [11] Rice, O. K. (1930). A contribution to the quantum mechanical theory of radioactivity and the dissociation by rotation of diatomic molecules. Physical Review, 35(12), 1538–1550. (URL:<https://doi.org/10.1103/physrev.35.1538>)
- [12] Zettili, N. (2022). Quantum Mechanics: Concepts and Applications. Wiley.
- [13] Glenn F. Knoll. Radiation interactions: Interaction of heavy charged particles. In Radiation detection and measurement, chapter 2, pages 30–34. Wiley, Hoboken, NJ, 4th edition, 2010. ISBN 978-0-470-13148-0.



- [14] Advanced Laboratory, Physics 407 (2010). Range of Alphas. University of Wisconsin. (URL:<https://www.physics.wisc.edu/courses/home/spring2018/407/experiments/alpha/newalpha.pdf>)
- [15] Canberra Industries (2006). Model 7401/7401VR Alpha Spectrometer. ISO 9001. (URL:[http://www.nuclearphysicslab.com/npl/wp-content/uploads/Canberra\\_7401-7401VR\\_Alpha\\_Spectrometer.pdf](http://www.nuclearphysicslab.com/npl/wp-content/uploads/Canberra_7401-7401VR_Alpha_Spectrometer.pdf))
- [16] "MathWorks: Histogram". (URL:<https://www.mathworks.com/help/matlab/ref/matlab.graphics.chart.primitive.histogram.html>)
- [17] ORTEC. Experiment 5: Energy Loss with Heavy Charged Particles (Alphas) (URL:<https://www.ortec-online.com/-/media/ametektortec/third-edition-experiments/5-energy-loss-heavy-charged-particles-alphas.pdf?la=en&revision=a52b68cc-788f-445d-93b6-520111f73d13&hash=9409314E5C3E9A42B72B95C5F347DB14>)

## Appendix A Neptunium Decay Series

Nuclide	Half life	$\alpha$ Energies (keV)	$P_\alpha$ (%)
<sup>241</sup> Am	432.6 a	5388	1.66
$\alpha$		5442.80	13.1
		5485.56	84.8
		5511.5	0.225
		5544.5	0.37
<sup>237</sup> Np	2.144 $\times 10^6$ a	4640.0	6.43
$\alpha$		4665.0	3.478
		4766.5	9.3
		4771.4	23.2
		4788.0	47.64
		4803.5	2.014
		4816.8	2.43
		4872.7	2.39
<sup>233</sup> Pa	26.974 d		
$\beta^-$			
<sup>233</sup> U	159.2 $\times 10^3$ a	4729.0	1.61
$\alpha$		4783.5	13.2
		4796.0	0.28
		4824.2	84.3
<sup>229</sup> Th	7340 a	4814.6	9.3
$\alpha$		4838.0	5.0
		4845.3	56.2
		4901.0	10.2
		4967.5	5.97
		4978.5	3.17
		5053.0	6.6
<sup>225</sup> Ra	14.9 d		
$\beta^-$			
<sup>225</sup> Ac	10.0 d	5732.0	8.0
$\alpha$		5790.6	8.6
		5792.5	18.1
		5830.0	50.7
<sup>221</sup> Fr	4.801 min	6126.3	15.1
$\alpha$		6241.8	1.36
		6341.0	83.3
<sup>217</sup> At	32.6 ms	7066.9	99.89
$\alpha$			
<sup>213</sup> Bi	45.59 min	5558	0.181
$\beta^-$ (97.86 %)		5875	1.959
<sup>209</sup> Tl	2.162 min		
$\beta^-$			
<sup>213</sup> Po	3.72 $\mu$ s	8376	100
$\alpha$			
<sup>209</sup> Pb	3.234 h		
$\beta^-$			
<sup>209</sup> Bi	1.9 $\times 10^{19}$ a	2877	1.2
$\alpha$		3077	98.8
<sup>205</sup> Tl	stable		

Figure 32: Neptunium Series, with  $\alpha$  particle energies and their emission probabilities  $P_\alpha$  [8]

## Appendix B Term Diagram of the Alpha Decay of Americium-241

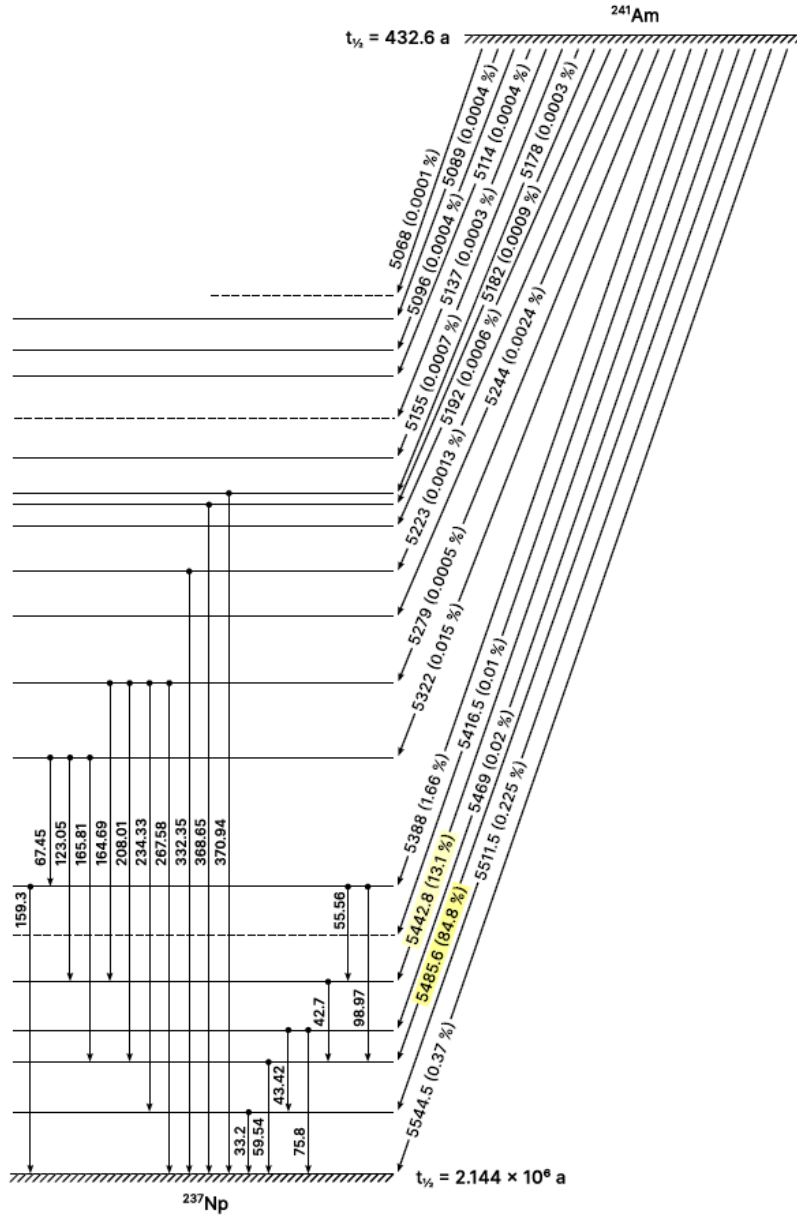


Figure 33: Term diagram of the  $\alpha$  decay of  $^{241}\text{Am}$ . Energies (in keV) of alpha particles (right) and of the gamma photons from the excited  $^{237}\text{Np}$  daughter nucleus (left). The probabilities of each decay is given in brackets [8]